Volume 26
Number 10
14 March 2024
Pages 7933–8560

PCCP

Physical Chemistry Chemical Physics

rsc.li/pccp

25 YEARS ANNIVERSARY

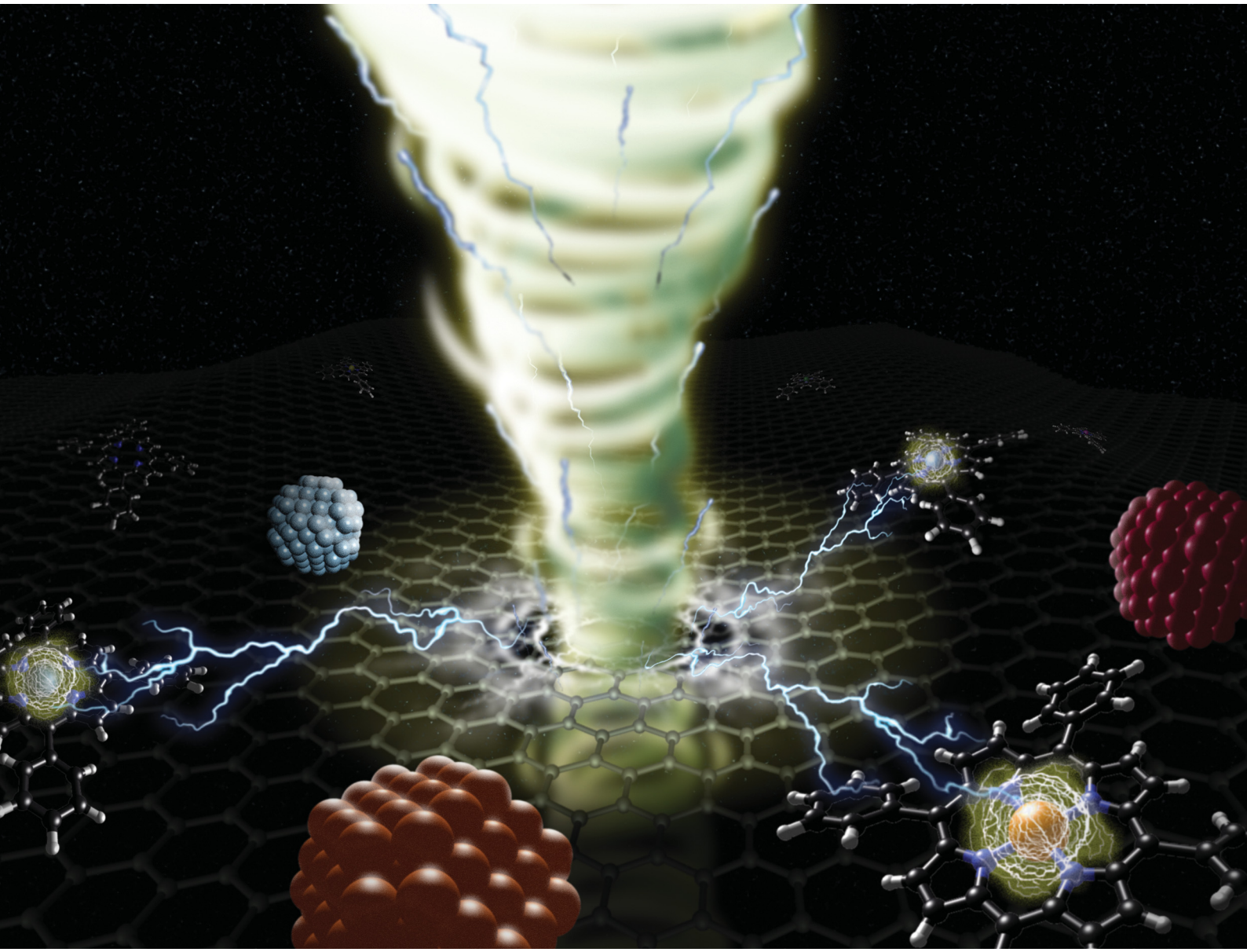

ISSN 1463-9076

ROYAL SOCIETY OF CHEMISTRY

PAPER

Dominik Lungerich *et al.*

Electron beam-induced demetallation of Fe, Co, Ni, Cu, Zn, Pd, and Pt metalloporphyrins: insights in e-beam chemistry and metal cluster formations

PCCP Owner Societies

PCCP

ROYAL SOCIETY OF CHEMISTRY

PAPER

View Article Online
View Journal | View Issue

Cite this: *Phys. Chem. Chem. Phys.*, 2024, **26**, 8051

Electron beam-induced demetallation of Fe, Co, Ni, Cu, Zn, Pd, and Pt metalloporphyrins: insights in e-beam chemistry and metal cluster formations†

Jongseong Park, [ab] Sol Lee,[a] Orein Francis Jafter, [ab] Jinwoo Cheon[abc] and Dominik Lungerich *[ab]

Received 30th November 2023,
Accepted 30th January 2024

DOI: 10.1039/d3cp05848d

rsc.li/pccp

Electron beams are versatile tools for nanoscale fabrication processes, however, the underlying e-beam chemistry remains in its infancy. Through *operando* transmission electron microscopy investigations, we elucidate a redox-driven cargo release of individual metal atoms triggered by electron beams. The chosen organic delivery molecule, tetraphenylporphyrin (**TPP**), proves highly versatile, forming complexes with nearly all metals from the periodic table and being easily processed in solution. A comprehensive cinematographic analysis of the dynamics of single metal atoms confirms the nearly instantaneous ejection of complexed metal atoms under an 80 kV electron beam, underscoring the system's broad versatility. Providing mechanistic insights, we employ density functional theory to support the proposed reductive demetallation pathway facilitated by secondary electrons, contributing novel perspectives to electron beam-mediated chemical reaction mechanisms. Lastly, our findings demonstrate that all seven metals investigated form nanoclusters once ejected from **TPP**, highlighting the method's potential for studying and developing sustainable single-atom and nanocluster catalysts.

Introduction

Recently, we published findings on the unexpected electron beam-induced demetallation of custom-made metallobenzoporphyrins deposited on graphene as a substrate.[1] While previous studies reported on the use of heavy transition metal contrast markers in molecular imaging by high-angle annular dark-field scanning transmission electron microscopy (HAADF-STEM),[2–6] our *operando* transmission electron microscopy (TEM) observations on metallobenzoporphyrins suggested that the metal atoms exhibited deficient complexation behavior by the macrocycle, once subjected to the electron beam (e-beam). This, in turn, is an opportunity for analyzing single metal atoms.

The investigation of single metal atom dynamics, encompassing their diffusion behavior on different substrates and the propensity to form larger aggregates and clusters, holds significant importance for various nanotechnological applications.[7,8] For instance, understanding the deactivation pathways of single-atom catalysts (SACs) is crucial for designing durable and sustainable catalysis solutions.[8,9] Likewise, in nanoelectronics, precise control over each atom's state is essential when they are implemented in single-atom transistors (SATs) for the fabrication of electronic quantum circuits.[10,11]

Apart from computational analysis of atom–substrate interactions, *in situ* TEM and respective single-molecule atomic-resolution time-resolved electron microscopy (SMART-EM) techniques stand out as powerful experimental tools for investigating ad-atom dynamics.[12–14] One way of depositing single metal atoms on substrates is using organic cargo-delivery molecules. As exemplified by Sinha *et al.*, Gd-atoms can be deposited on graphene by drop-casting a solution of $Gd_3N@C_{80}$ endohedral metallofullerenes (EMFs), followed by the release of the metal atoms onto the substrate upon annealing to 900 °C.[15] While this cargo methodology is elegant, its limitation to only a few and expensive EMFs poses a challenge.

In this work, we present a generalized approach for the redox-driven cargo release of solution-based single-metal-atom deposition on graphene. Therefore, we employed the widely accessible tetraphenylporphyrin (**TPP**) as a redox-active macrocyclic ligand for transition metals, which upon e-beam irradiation, releases the complexed metal atoms and subsequently form metal clusters (Scheme 1). By studying seven different

[a] *Center for Nanomedicine, Institute for Basic Science (IBS), Seoul 03722, Republic of Korea*
[b] *Department of Nano Biomedical Engineering (NanoBME), Advanced Science Institute, Yonsei University, Seoul 03722, Republic of Korea. E-mail: d.lungerich@yonsei.ac.kr*
[c] *Department of Chemistry, Yonsei University, Seoul 03722, Republic of Korea*

† Electronic supplementary information (ESI) available. See DOI: https://doi.org/10.1039/d3cp05848d

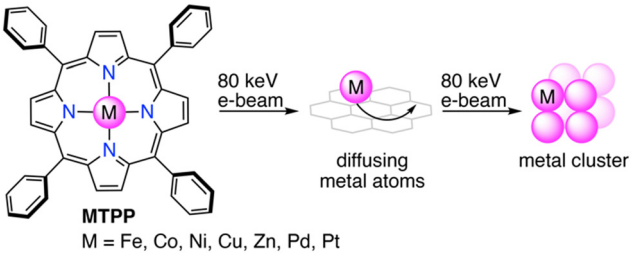

Scheme 1 Redox-driven cargo release of single metal atoms from metalloporphyrins and formation of metal clusters.

metalloporphyrins (Fe, Co, Ni, Cu, Zn, Pd, and Pt), we elucidate herein the e-beam chemistry of metalloporphyrins through *operando* (scanning) transmission electron microscopy, complemented by energy-dispersive X-ray spectroscopy (EDS) and density functional theory (DFT).

Experimental

Synthesis of metallotetraphenylporphyrins

Chemicals were purchased from Sigma-Aldrich and used without any further purification. CH_2Cl_2 was neutralized with K_2CO_3 and distilled prior to usage. Reactions were carried out in darkness and under a dry argon atmosphere using standard Schlenk techniques. Reaction vessels were heated with polymer-coated heat-on blocks. All synthetic and structural characterizations are described in detail in the ESI.† Briefly, the **MTPP**s were synthesized from **TPP**, as shown in Fig. 1a, following the protocols described below. Absorption spectra of the synthesized **MTPP**s are shown in Fig. 1b.

FeTPP. TPP (100 mg, 163 μmol) and $FeCl_2$ (309 mg, 2.45 mmol) were dissolved in DMF (40 mL) and brought to reflux for 5 h. The mixture was plug filtered (SiO_2; MeOH/Hex/EtOAc (1 : 1 : 1)) and concentrated. The crude was purified by column chromatography (SiO_2; EtOAc/Hex (1 : 1)) and precipitated from MeOH with H_2O to give the product as a dark-brown colored solid in 64% (70 mg, 100 μmol) yield.

CoTPP. TPP (100 mg, 163 μmol) and $Co(OAc)_2{\cdot}2H_2O$ (288 mg, 1.63 mmol) were dissolved in THF (50 mL), and the mixture was brought to reflux for 20 h. The mixture was plug filtered (SiO_2; CH_2Cl_2/Hex (1 : 1)) and precipitated from CH_2Cl_2 with MeOH to give the product as a burgundy-colored solid in 57% (62 mg, 93.0 μmol) yield.

NiTPP. TPP (50 mg, 81.3 μmol) and $Ni(acac)_2$ (209 mg, 813 μmol) were dissolved in toluene (25 mL) and brought to reflux for 24 h. The mixture was plug-filtered (SiO_2; toluene), concentrated, and precipitated from toluene with MeOH. The solid was filtered, washed with MeOH, and dried in vacuum to give the product as a purple solid in 46% (25 mg, 37.2 μmol) yield.

CuTPP. TPP (50 mg, 81.3 μmol) dissolved in CH_2Cl_2 (50 mL) was charged with a saturated solution of $Cu(OAc)_2{\cdot}H_2O$ in MeOH (5 mL) and stirred for 20 h at rt. The mixture was plug filtered (SiO_2; CH_2Cl_2), concentrated, and purified by column chromatography (SiO_2; CH_2Cl_2/Hex (1 : 1)). The product was precipitated from CH_2Cl_2 with MeOH to give a red-colored solid in 97% (53 mg, 79 μmol) yield.

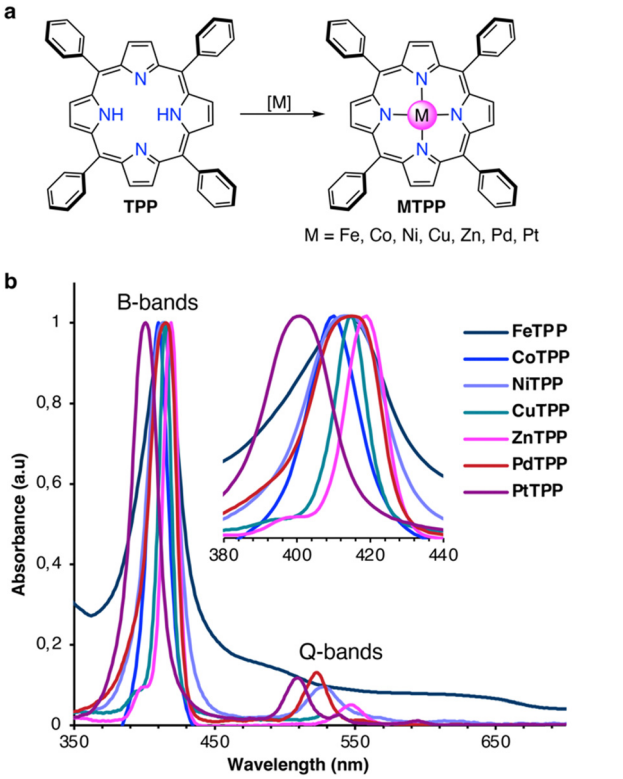

Fig. 1 (a) Synthesis of **MTPP**s from **TPP**. (b) Normalized UV/Vis absorption spectra of **MTPP**s in CH_2Cl_2 at rt.

ZnTPP. TPP (60 mg, 98.0 μmol) dissolved in CH_2Cl_2 (50 mL) was charged with a saturated solution of $Zn(OAc)_2$ in MeOH (5 mL) and stirred for 20 h at rt. The mixture was plug filtered (SiO_2; CH_2Cl_2), concentrated, and purified by column chromatography (SiO_2; CH_2Cl_2/Hex (1 : 1)). The product was precipitated from CH_2Cl_2 with MeOH to give a pink-colored solid in 72% (48 mg, 71 μmol) yield.

PdTPP. $PdCl_2$ (289 mg, 1.63 mmol) was dissolved in benzonitrile (25 mL) and brought to reflux for 30 min. **TPP** (100 mg, 163 μmol) was added as a solid, and the mixture was brought to reflux for 6 h. The solvent was distilled off, the mixture was plug-filtered (SiO_2; toluene), concentrated, and precipitated from toluene with MeOH. The solid was filtered, washed with MeOH, and dried in vacuum to yield the product as a red solid in 70% (82 mg, 114 μmol) yield.

PtTPP. $Pt(acac)_2$ (641 mg, 1.63 mmol) was dissolved in benzonitrile (25 mL) and brought to reflux for 30 min. **TPP** (100 mg, 163 μmol) was added as a solid, and the mixture was brought to reflux for 6 h. The solvent was distilled off, the mixture was plug-filtered (SiO_2; toluene), concentrated, and precipitated from toluene with MeOH. The solid was filtered, washed with MeOH, and dried in vacuum to yield the product as a red solid in 60% (80 mg, 97.8 μmol) yield.

Graphene grid preparation

Graphene was synthesized *via* chemical vapor deposition (CVD) on 25 μm Cu foils (99.8%, Alfa Aesar).[16] An illustration of the graphene transfer steps onto TEM grids is presented in Fig. S1

in the ESI.† Briefly, graphene on the back side of the Cu foil was etched by O_2 plasma in the reactive-ion etching (RIE) mode (CUTE, Femto Science Co.) (power = 70 W, flow rate = 20 sccm). Polymethyl methacrylate (PMMA) solution (PMMA-950 K A4, MicroChem Corp.) was spin-coated on graphene/Cu foils at 3000 rpm for 1 min and dried in air. The copper foil was etched with an aqueous 2 mM ammonium persulfate [$(NH_4)_2S_2O_8$] solution for 24 h. The PMMA/graphene stacks were rinsed three times in deionized water. The stacks were scooped onto Quantifoil holey carbon TEM grids (R2/2 400 mesh Gold, SPI Supplies Inc.) and dried in air for 24 h. To enhance the adhesion between graphene and the carbon film of the TEM grids, PMMA/graphene/grids were heated at 150 °C for 10 min. Finally, the PMMA film was dissolved with acetone.[17]

(S)TEM analysis and data processing

Atomic-resolution *operando* electron microscopy was carried out on a cold FEG JEOL JEM-ARM200F instrument equipped with a double Cs aberration corrector and double JED-2300T energy-dispersive X-ray spectrometer at an acceleration voltage of 80 kV and a vacuum of 1×10^{-5} Pa in the TEM column. TEM, STEM, and EDS elemental mapping experiments were carried out on a reinforced beryllium double tilt holder (JEOL EM-01360RSTHB) at rt. TEM videos were recorded on a CMOS camera (Gatan OneView-IS, 2048 × 2048 pixels) operated in binning 1 mode (output image size 2048 × 2048 pixels, with a pixel resolution of 0.01 nm at ×2 000 000), an exposure time of 40 ms, and a frame rate of 25 fps. All images were automatically processed using Gatan DigitalMicrograph software. HAADF-STEM camera lengths of 6 and 8 cm (with detection angles ranging from 90 to 370 mrad and 68 to 280 mrad, respectively) were used. The probe size was 6 and 7C (120 and 60 pA, respectively), and the condenser lens (CL) aperture size was 40 μm. The probe convergence angle was between 28 to 33 mrad. Images were collected in the .dm4 format on Gatan DigitalMicrograph software and processed using ImageJ 1.54f software.[18] Images were subjected to thermal drift correction, and Gaussian blurred before analysis. Trajectories of single metal atoms and clusters were tracked and analyzed with TrackMate as implemented in Fiji.[19,20] Electron diffraction pattern was simulated using the SingleCrystal software (CrystalMaker Software Ltd). TEM simulation images were generated using a multi-slice procedure implemented in Bionet elbis software.[21] Simulation parameters were set to agree with the actual experimental parameters: acc. volt. = 80.00 kV, λ = 0.04176 Å, C_s = −0.00490 mm, d_f = 129.49 Å, C_c = 0.25 mm, d_e = 0.43 eV, α = 0.20 mrad, OL aperture radius = 20.88 mrad, OL aperture radius = 0.50 $Å^{-1}$, pixel size = 0.1089 Å, max. intens. = 1.5165.

DFT calculations

Geometry optimization and energy calculations were performed on Q-Chem as implemented in the SPARTAN '20 work package.[22–24] Structures were first optimized using the semi-empirical method PM6,[25] followed by the Head Gordon range-separated global hybrid generalized gradient approximation density functional ωB97X-D with Grimme D2 dispersion correction,[26,27] using the Pople-type double-ζ split-valence basis set 6-31G(d).[28–30] To reduce calculation costs, the *meso*-phenyl rings were replaced by hydrogen atoms to represent metalloporphins (**MP**s). Single-point calculations were obtained at the triple-ζ 6-311+G(2df,2p) level of theory.[31,32] Ionization energies were obtained from the frozen geometry of the neutral molecule in the respective ionization state, whereby possible, the electronic closed-shell configurations were considered. Threshold displacement energies E_d were determined at the ωB97X-D/6-311G(2d,p)//B3LYP/6-31G(d) level of theory. E_d was obtained from the Morse potential calculations for the gradual extension over 20 steps of the respective N_4–M bonds from equilibrium distance to a length of 7 Å. The intersection of the slopes for the binding potential (equilibrium −2.8 Å) and the non-binding potential (4–7 Å) resulted in the determined threshold energies for the homolytic bond scissions at different redox states.[1,17]

Results and discussion

Diffusion of single metal atoms

For this generalization study of the redox-driven cargo release of single metal atoms, we decided to investigate the catalytically active group ten elements Ni, Pd, and Pt, as well as the neighboring transition metals from the fourth period, Fe, Co, Cu, and Zn, to have a comprehensive view on the goings-on under the e-beam. We drop-casted 10 μL of a 1.5 mM solution of the **MTPP**s in tetrahydrofuran (THF) (Fig. 2a) on the freshly prepared graphene grids, and excess of the solution was removed with a blotting paper as illustrated in Fig. 2b. The grids were then dried in vacuum (10^{-3} mbar) before being subjected to TEM analysis. Compared to previously published metal atom deposition techniques, such as thermal evaporation,[33] e-beam deposition,[34] soft-landing deposition,[35] atomic layer deposition,[36] chemical vapor deposition,[37] or magnetron sputtering,[38] our solution-based deposition is a highly versatile and easily accessible method that does not require any additional equipment.

We initiated our investigation with **PtTPP**, which features the Pt in the +II oxidation state. Upon examining the substrate for pristine graphene regions at high magnifications (×2 000 000) with a moderate electron flux of $\sim 10^{-6}$ e^- nm^{-2} s^{-1} for SMART-EM studies,[39–44] we discovered omnipresent single Pt atoms. As highlighted in the time-dependent image sequence of two Pt atoms in Fig. 3a (Video S1, ESI†), dynamic behavior for both atoms was observed, as evidenced by the diffusion trajectories. Hereby, Pt atom 1, which was situated on the graphene monolayer at the edge of an amorphous carbon layer showed an increased translational mobility compared to Pt atom 2, which was embedded in the amorphous carbon layer and only moving due to dynamic changes of the layer (Fig. 3b). The omnipresent amorphous carbon islands on the graphene surface are residues from the graphene grid fabrication (compare also Fig. S2 in the ESI†).[45–47]

This dynamic behavior of single metal atoms was also observed when other **MTPP**s (M = Fe, Co, Ni, Cu, Zn, and Pd)

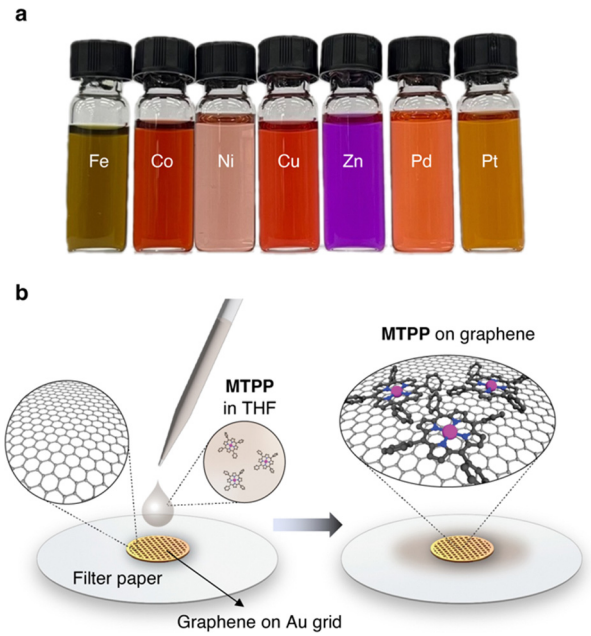

Fig. 2 TEM Sample preparation. (a) Image of the used 1.5 mM solutions of **MTPP**s in THF. (b) Illustration of the solution-based deposition of **MTPP**s on the graphene grid.

were used, as summarized in Fig. 3c, unequivocally indicating a successful demetallation of all **MTPP**s under the electron beam. Notably, all metals within the **MTPP**s are present in the +II oxidation state; only in the case of **FeTPP** does the iron carry a fifth ligand (chloro) and is, therefore, in the +III oxidation state. Nonetheless, Fe is equally well demetallated compared to the +II metals. The dynamics of the metal atoms align with previous *in situ* TEM studies on single metal atoms,[7,48–50] confirming that the demetallation pathway utilized herein yields comparable results to previously published deposition methods.

Regarding general chemical demetallation strategies of porphyrins, **ZnTPP** is routinely demetallated under wet-chemical conditions with mild acids, which makes demetallation induced by diffusing H^+ atoms, in principle, plausible. On the other hand, derivatives like **NiTPP** exhibit a high resistance to acid-mediated demetallation and necessitate alternative strategies, such as reductive demetallation with Grignard reagents.[51–53] This observation provides valuable insights into the demetallation mechanisms (*vide infra*). Further, at the employed electron flux, a metal release due to critical fragmentations of the *meso* or α-carbons in the **TPP** ligand is earliest expected to proceed after ~30 s; however, the metal atoms were immediately detected upon scanning the surface, rendering a fragmentation-induced metal release less likely (*vide infra*).[1]

Theoretical evaluation

To rationalize the mechanism of the observed demetallation, we considered beam-molecule interactions based on elastic and inelastic scattering events.[54] In the case of elastic scattering, the electrons are deflected from their trajectory through attractive Coulomb interactions between the positively charged nucleus and the beam electrons. During this process, momentum is transferred to the nucleus, which causes a translation of the atom from its equilibrium position. As a consequence, the atoms in the molecules vibrate and are thus lifted into vibronically excited states. If the transferred kinetic energy exceeds the threshold displacement energy E_d of the atom in the molecule, this vibronic excitation can terminate in a homolytic bond cleavage and a fragmentation of the molecule occurs.[55] Herein, we will denote the non-destructive e-beam-induced vibronic excitation of molecular bonds, induced by elastic scattering, as 'knock-on excitation', whereas the destructive bond cleavage will be termed 'knock-on displacement'.

The transferred kinetic energy E_T to the nucleus can be calculated according to eqn (1), where E_0 is the intrinsic kinetic energy of the electron, A is the atomic mass number, and θ is

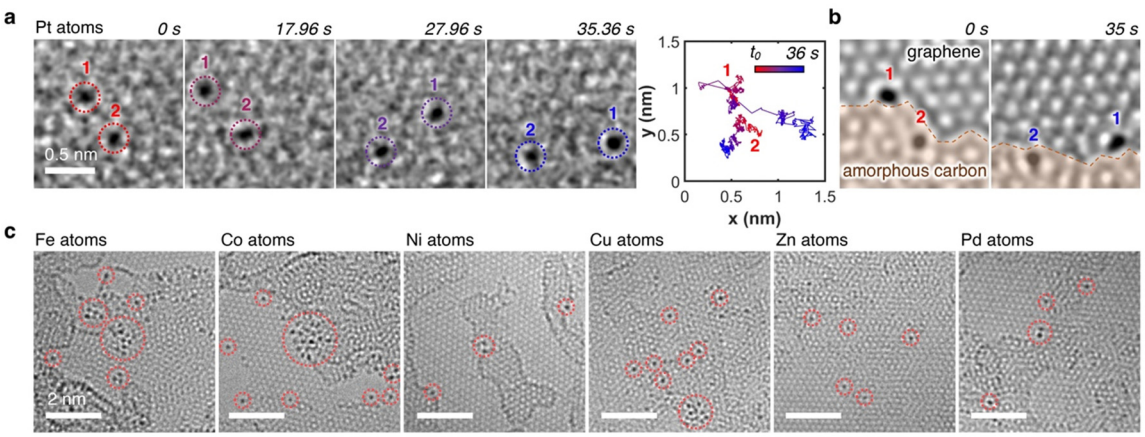

Fig. 3 Released single metal atoms. (a) Time-dependent sequence of two Pt atoms. The coloration of the metal atoms corresponds to the time stamp from the respective trajectories. (b) Images of stacked sequence (25 frames corresponding to 1 s exposure time), highlighting the location of each atom. Atom 1 is located on the graphene monolayer at the edge of an amorphous carbon layer; atom 2 is embedded within the amorphous carbon layer. (c) Overview images of remaining single metal atoms (Fe, Co, Ni, Cu, Zn, Pd) released by the e-beam.

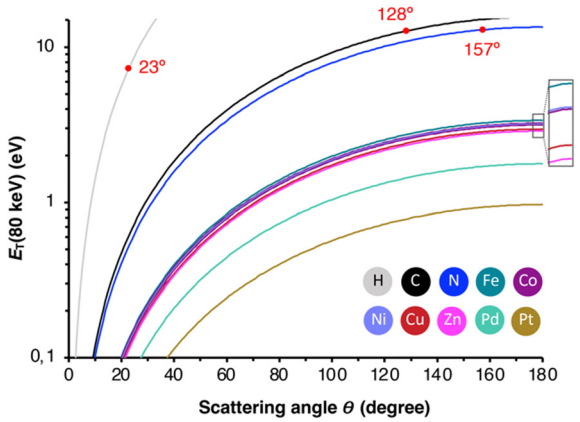

Fig. 4 Transferred energy E_T against the elastic scattering angle Θ for all studied elements. In red are the angles indicated, at which E_T exceeds E_d.

the scattering angle.[56]

$$E_T = \frac{E_0\left(1.02 + \frac{E_0}{10^6}\right)}{465.7A}\sin^2\frac{\theta}{2} \quad (1)$$

At a scattering angle of 180°, the transferred energy is at its maximum (E_{max}). If E_T exceeds E_d, knock-on displacement can occur. As indicated in Fig. 4, only light elements, including H, C, and N, can receive enough momentum to result in a bond cleavage. All investigated metals do not receive enough momentum to be displaced from the molecule. While a scattering angle of only 23° is necessary to displace hydrogen from **MTPP**, it should be noted that the cross-section for this event is relatively low 5.2 × 10^{-6} a_0^2 sr^{-1} (carbon: 5.1 × 10^{-7} a_0^2 sr^{-1}; nitrogen: 2.5 × $10^{-7}a_0^2$ sr^{-1}; compare Fig. S3 in the ESI†).[57] Nonetheless, C–H bond cleavages are expected to occur after prolonged irradiation. These fragmented hydrogen atoms can have a high enough kinetic energy to be transferred to the atoms, denoted as $E_{H\text{-}flux}$.[40] As listed in Table 1, $E_{H\text{-}flux}$ is high enough to remove most metals from the porphyrins; however, it is not large enough to demetallate **PdTPP** and **PtTPP**. Additionally, the probability of this cascade reaction occurring is substantially reduced as opposed to electron-driven processes and, therefore, is unlikely to be the main driving force for the rapid demetallation process.

Table 1 Summaries on calculated energies involved during elastic scattering processes

Element	E_{max} (80 keV)/eV	$E_{H\text{-}flux}$/eV	E_d/eV	σ^1_{KO} (80 keV)/barn
H	187.5	187.5	7.73	66
C	15.73	53.57	12.70	20
N	13.49	46.97	12.95	4.5
Fe	3.38	13.06	10.91	0
Co	3.21	12.40	9.50	0
Ni	3.22	12.45	10.23	0
Cu	2.97	11.53	7.24	0
Zn	2.89	11.21	6.80	0
Pd	1.78	6.97	8.08	0
Pt	0.97	3.84	10.38	0

Table 2 Vertical ionization energies of **MTPP**s calculated at the wB97X-D/6-311+G(2df,2p) level of theory

	$\Delta E_{ionization}$/eV			
Metal	$[MTPP]^{2+}$	$[MTPP]^{+}$	$[MTPP]^{-}$	$[MTPP]^{2-}$
Fe	17.49	7.97	−2.77	1.05
Co	17.44	9.51	−0.92	1.54
Ni	18.10	6.90	−0.78	1.46
Cu	18.33	7.94	−0.67	1.65
Zn	17.58	6.73	−1.28	1.32
Pd	17.80	6.83	−1.26	1.33
Pt	17.89	6.87	−1.20	1.38

Alternatively, inelastic scattering events, which stem from electron–electron interactions, where the beam-electron donates a substantial amount of energy to the electrons of the molecules, were considered. The probability for inelastic scattering to occur is several magnitudes larger (~10^5) than for elastic scattering processes, which renders it likely the initial driving force behind the demetallation.[58–60] Thus, we evaluated the oxidation and reduction of metalloporphyrins employing DFT calculations. As summarized in Table 2, the one and two-electron oxidation of metalloporphyrins is energetically demanding. In contrast, the one-electron and, to a lesser extent, the two-electron reduction are energetically feasible. Hence, we determined E_d for the $N_4\cdots M$ bond cleavage, as summarized in Table 1 and depicted in the form of the Morse potentials in Fig. 5a. As shown, **ZnP** exhibits the weakest metal complexation, whereas **FeP**, **PtP**, and **NiP** exhibit the strongest complexations. These calculations agree well with wet-chemical complexation stabilities, as discussed above. Notably, the complexation affinity is strongly altered upon ionization of the molecule. As exemplified for **ZnP** in Fig. 5b, reduction to $\mathbf{ZnP}^-$ and $\mathbf{ZnP}^{2-}$ leads to a decrease in binding strength, whereas oxidation to $\mathbf{ZnP}^+$ and $\mathbf{ZnP}^{2+}$ has the inverse effect (the remaining Morse potentials are displayed in Fig. S9 in the ESI†). This behavior is well reflected in reports about the wet-chemical reductive demetallation of porphyrins.[52,53]

Therefore, we propose that the demetallation is driven by omnipresent secondary electrons (SEs), which can reduce metalloporphyrins through electron attachment. Subsequent vibronic excitations, enhanced by elastic scattering, lead to the rapid ejection of the complexed metal atoms, as depicted in Fig. 5c (further mechanistic explanations are depicted in Fig. S8 in the ESI†). This pathway explains why metal atoms are already found to be displaced when screening the surface without being exposed to prolonged e-beams, as SEs are ejected into the periphery of the primary electron beam (beam shadow).[1] At the same time, this effect is enhanced in thicker samples as more SEs are generated. Consequently, using (S)TEM for molecular structure determination, using a low electron flux, thin samples to reduce the formation of SEs, and a conductive specimen to facilitate charge recombination processes, is critical.[5]

Formation and dynamics of metal clusters

In regions characterized by a high concentration of metal atoms, a tendency towards cluster formation under the e-beam in TEM mode was evident. Fig. 6a (Video S2, ESI†) illustrates three

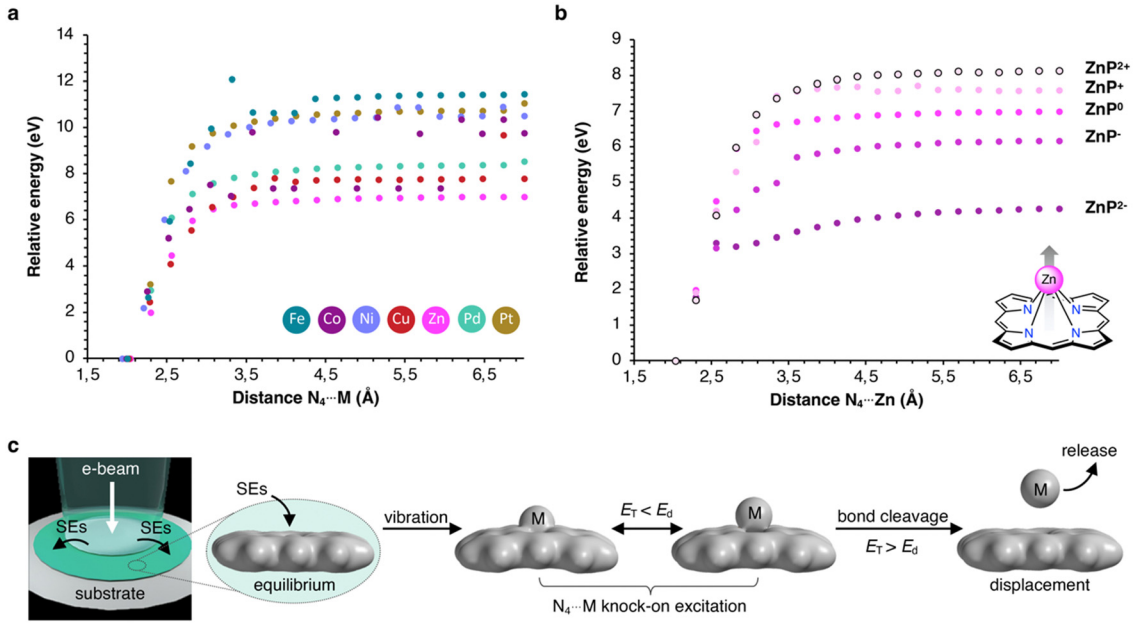

Fig. 5 Evaluation of the homolytic bond cleavage of the $N_4\cdots M$ bond in metalloporphins **MP**s. (a) Morse potential curves for all **MP**s in the neutral state. (b) Exemplified Morse potential of **ZnP** in different ionization states (−2, −1, 0, +1, +2). (c) Proposed demetallation mechanism induced by secondary electrons (SEs). Electron density maps of **ZnP** models at increasing bond length are calculated at the ωB97X-D/6-311G(2d,p) level of theory; iso-value of electron density shows a 95% electron probability (0.0164 e^- a.u.$^{-3}$).

amorphous Pt clusters, each approximately 1 nm in size, maintaining mobility despite their dimensions. 60 s after t_0, two of the three clusters coalesced. 28 s later, this fused cluster approached the remaining one, culminating into a single amorphous cluster. Positioned on an amorphous carbon layer, these clusters traversed a distance of about 3 nm over a 100 s duration, converging into a single amorphous Pt cluster, as depicted in the trajectory plot in Fig. 6a. Even in a crystalline state, metal atoms exhibited mobility under electron beam irradiation, which support the formation of flexible metal clusters rather than rigid metal carbides,[61,62] as exemplified by an image sequence of a Ni cluster in Fig. 6b (Video S3, ESI†). Adopting a body-centered cubic (BCC) packing unit, the Ni atoms continually rearranged themselves in response to the electron beam. Notably, the small Ni cluster stabilized in the BCC packing due to its high surface-to-volume ratio, whereas larger crystals usually favor a

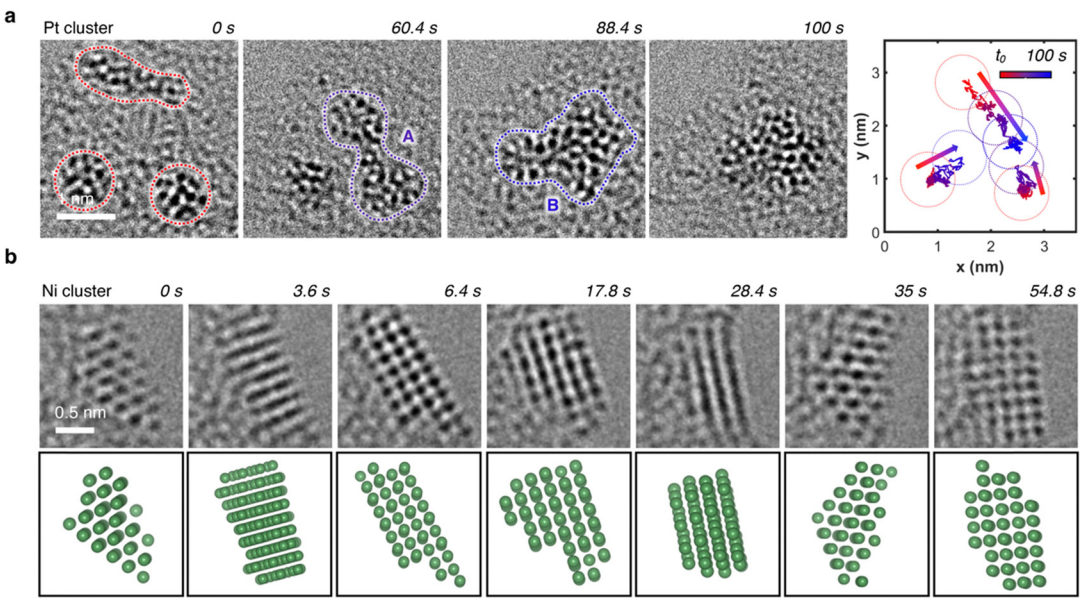

Fig. 6 TEM mode analysis of metal cluster dynamics. (a) Merging of three amorphous Pt clusters over a time period of 100 s. The moment of initial coalescence is indicated by (A) and the final by (B). (b) Atomistic rearrangement in a crystalline Ni cluster in the BCC packing over a time period of 55 s.

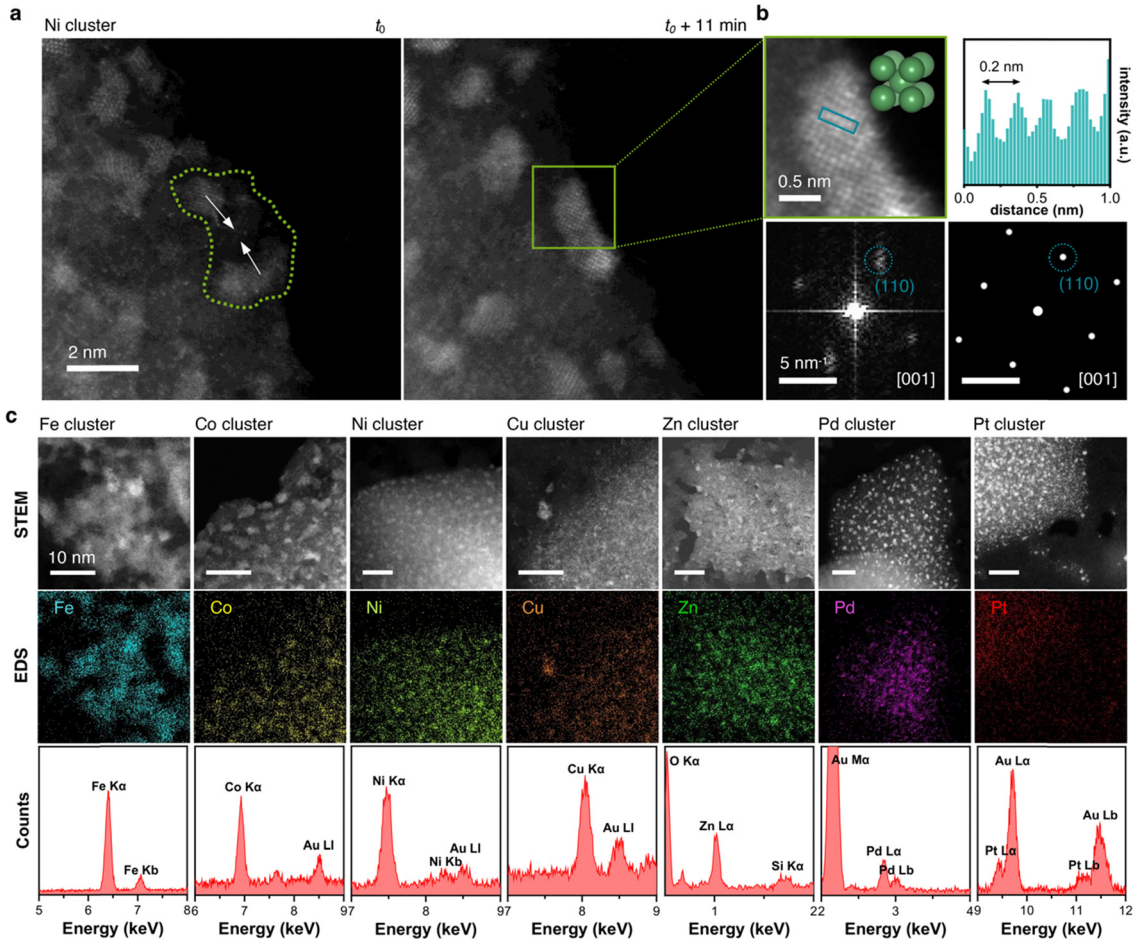

Fig. 7 STEM mode analysis of metal clusters. (a) HAADF-STEM images of the coalescing crystalline Ni clusters upon irradiating the area in STEM mode for 11 min. (b) Magnified HAADF-STEM image of the BCC Ni crystal, the measured plot profile and experimental FFT (left) and simulated (right) diffraction pattern. (c) HAADF-STEM images and EDS mapping of all investigated metals (Fe, Co, Ni, Cu, Zn, Pd, Pt) and clusters.

face-centered cubic (FCC) motif.[63,64] The metastable BCC crystal packing persisted throughout the video sequence, with only the crystal's shape and orientation on the substrate evolving over time.

To discern whether the electron beam in STEM mode also induced dynamic atomistic changes, we investigated various areas with metal clusters, as exemplified by Ni clusters in Fig. 7a. Highlighted in the green area, at t_0, the two clusters were distinctly separated by approximately 2 nm. Under continuous scanning e-beam irradiation over 11 minutes, both clusters translated on the surface and merged into a single crystalline Ni cluster. Examination of the cluster highlighted in the green box in Fig. 7b revealed a Ni crystal exhibiting 0.2 nm interatomic distances. Further analysis of the Fast Fourrier Transform (FFT) pattern correlates with the peak (011) along the [100] plane, which agrees well with the simulated diffraction pattern for Ni's BCC structure. Ultimately, as evidenced by HAADF-STEM and EDS mapping images in Fig. 7c, cluster formations were observed for all seven metals investigated herein, underscoring the general applicability of **MTPP**s as redox-driven cargo delivery systems for the generation of nanoclusters under the electron beam.

Conclusions

In this work, we present a straightforward and widely applicable approach for the solution-based deposition and electron beam-triggered liberation of individual metal atoms onto carbon substrates. Significantly, we employ readily available organic cargo-delivery systems, specifically tetraphenylporphyrins, which form complexes with a broad spectrum of transition and main group metals, imparting exceptional versatility to these molecules. Through *operando* transmission electron microscopy, we illustrate the characteristic surface mobility of the metal atoms, indicating their release from the molecular complexes. Density functional theory calculations support our observation that the rapid metal release is attributed to a reductive demetallation pathway induced by secondary electrons rather than physical fragmentation of the macrocycle through knock-on displacement. As a consequence, decreasing the acceleration voltage will increase the secondary electron formation and subsequently increase the demetallation process. This mechanistic insight contributes to the understanding of electron beam-initiated chemical reaction mechanisms, an area that remains largely unexplored.[17,59,60,65]

Notably, our method exhibits high versatility by operating at room temperature without the necessity for annealing, hydrogenation, or any pre-treatment. Thus, through redox-driven cargo release, we demonstrate a methodology for e-beam-synthesized metallic nanoclusters for diverse applications, such as catalysis. Furthermore, the facile implementation of heteroatoms on the substrate, such as nitrogen, can be envisioned through additional molecular engineering of the porphyrin's periphery.[66–70] Incorporating heteroatom-rich substituents allows for precise modulation of material properties, potentially serving as dopants or anchor points within the substrate, thereby offering a means to fine-tune the materials as needed.

Author contributions

D. L. conceived the project and supervised it with J. C. J. P. carried out electron microscopy experiments and data analysis with the help of S. L. S. L. prepared the graphene grids. O. F. J. synthesized and characterized the metalloporphyrins. D. L. wrote the manuscript with the help of J. P., S. L., and O. F. J. All authors discussed the results.

Conflicts of interest

There are no conflicts to declare.

Acknowledgements

This research was supported by the Institute for Basic Science (IBS-R026-Y1, IBS-R026-D1). Professor Eiichi Nakamura and Professor Koji Harano (University of Tokyo) are thanked for their valuable discussions of the involved mechanisms and for supporting initial SMART-EM experiments.

Notes and references

1 H. Hoelzel, S. Lee, K. Y. Amsharov, N. Jux, K. Harano, E. Nakamura and D. Lungerich, Time-resolved imaging and analysis of the electron beam-induced formation of an open-cage metallo-azafullerene, *Nat. Chem.*, 2023, **15**, 1444–1451.

2 M. A. Gerkman, S. Sinha, J. H. Warner and G. G. D. Han, Direct Imaging of Photoswitching Molecular Conformations Using Individual Metal Atom Markers, *ACS Nano*, 2019, **13**, 87–96.

3 E. S. Kengmana, J. K. Lee, X. Li, J. H. Warner and G. G. D. Han, Self-Assembly of Bowlic Supramolecules on Graphene Imaged at the Individual Molecular Level using Heavy Atom Tagging, *Small*, 2020, **16**, e2002860.

4 E. Kano, M. Takeguchi, J. Fujita and A. Hashimoto, Direct observation of Pt-terminating carbyne on graphene, *Carbon*, 2014, **80**, 382–386.

5 P. Kharel, B. E. Janicek, S. Hyun Bae, A. L. Loutris, P. T. Carmichael and P. Y. Huang, Atomic-Resolution Imaging of Small Organic Molecules on Graphene, *Nano Lett.*, 2022, **22**, 3628–3635.

6 J. K. Lee, I. Bulut, M. Rickhaus, Y. Sheng, X. Li, G. G. D. Han, G. A. D. Briggs, H. L. Anderson and J. H. Warner, Metal Atom Markers for Imaging Epitaxial Molecular Self-Assembly on Graphene by Scanning Transmission Electron Microscopy, *ACS Nano*, 2019, **13**, 7252–7260.

7 I. Popov, S. Ghaderzadeh, E. C. Kohlrausch, L. T. Norman, T. J. A. Slater, G. N. Aliev, H. Alhabeadi, A. Kaplan, W. Theis, A. N. Khlobystov, J. A. Fernandes and E. Besley, Chemical Kinetics of Metal Single Atom and Nanocluster Formation on Surfaces: An Example of Pt on Hexagonal Boron Nitride, *Nano Lett.*, 2023, **23**, 8006–8012.

8 I. H. Kim, J. Lim and S. O. Kim, Discovery of Single-Atom Catalyst: Customized Heteroelement Dopants on Graphene, *Acc. Mater. Res.*, 2021, **2**, 394–406.

9 X. He, Y. Deng, Y. Zhang, Q. He, D. Xiao, M. Peng, Y. Zhao, H. Zhang, R. Luo, T. Gan, H. Ji and D. Ma, Mechanochemical Kilogram-Scale Synthesis of Noble Metal Single-Atom Catalysts, *Cell Rep. Phys. Sci.*, 2020, **1**, 100004.

10 C. Schirm, M. Matt, F. Pauly, J. C. Cuevas, P. Nielaba and E. Scheer, A current-driven single-atom memory, *Nat. Nanotechnol.*, 2013, **8**, 645–648.

11 M. Fuechsle, J. A. Miwa, S. Mahapatra, H. Ryu, S. Lee, O. Warschkow, L. C. L. Hollenberg, G. Klimeck and M. Y. Simmons, A single-atom transistor, *Nat. Nanotechnol.*, 2012, **7**, 242–246.

12 K. Cao, J. Biskupek, C. T. Stoppiello, R. L. McSweeney, T. W. Chamberlain, Z. Liu, K. Suenaga, S. T. Skowron, E. Besley, A. N. Khlobystov and U. Kaiser, Atomic mechanism of metal crystal nucleus formation in a single-walled carbon nanotube, *Nat. Chem.*, 2020, **12**, 921–928.

13 K. Cao, T. Zoberbier, J. Biskupek, A. Botos, R. L. McSweeney, A. Kurtoglu, C. T. Stoppiello, A. V. Markevich, E. Besley, T. W. Chamberlain, U. Kaiser and A. N. Khlobystov, Comparison of atomic scale dynamics for the middle and late transition metal nanocatalysts, *Nat. Commun.*, 2018, **9**, 3382.

14 K. Cao, S. T. Skowron, J. Biskupek, C. T. Stoppiello, C. Leist, E. Besley, A. N. Khlobystov and U. Kaiser, Imaging an unsupported metal–metal bond in dirhenium molecules at the atomic scale, *Sci. Adv.*, 2020, **6**, eaay5849.

15 S. Sinha, Y. Sheng, I. Griffiths, N. P. Young, S. Zhou, A. I. Kirkland, K. Porfyrakis and J. H. Warner, In Situ Atomic-Level Studies of Gd Atom Release and Migration on Graphene from a Metallofullerene Precursor, *ACS Nano*, 2018, **12**, 10439–10451.

16 X. Li, W. Cai, J. An, S. Kim, J. Nah, D. Yang, R. Piner, A. Velamakanni, I. Jung, E. Tutuc, S. K. Banerjee, L. Colombo and R. S. Ruoff, Large-Area Synthesis of High-Quality and Uniform Graphene Films on Copper Foils, *Science*, 2009, **324**, 1312–1314.

17 D. Lungerich, H. Hoelzel, K. Harano and N. Jux, K. Yu. Amsharov and E. Nakamura, A Singular Molecule-to-Molecule Transformation on Video: The Bottom-Up Synthesis of Fullerene C60 from Truxene Derivative C60H30, *ACS Nano*, 2021, **15**, 12804–12814.

18 C. A. Schneider, W. S. Rasband and K. W. Eliceiri, NIH Image to ImageJ: 25 years of image analysis, *Nat. Methods*, 2012, **9**, 671–675.

19 J.-Y. Tinevez, N. Perry, J. Schindelin, G. M. Hoopes, G. D. Reynolds, E. Laplantine, S. Y. Bednarek, S. L. Shorte and K. W. Eliceiri, TrackMate: an open and extensible platform for single-particle tracking, *Methods*, 2017, **115**, 80–90.

20 D. Ershov, M.-S. Phan, J. W. Pylvänäinen, S. U. Rigaud, L. L. Blanc, A. Charles-Orszag, J. R. W. Conway, R. F. Laine, N. H. Roy, D. Bonazzi, G. Duménil, G. Jacquemet and J.-Y. Tinevez, TrackMate 7: integrating state-of-the-art segmentation algorithms into tracking pipelines, *Nat. Methods*, 2022, **19**, 829–832.

21 F. Hosokawa, T. Shinkawa, Y. Arai and T. Sannomiya, Benchmark test of accelerated multi-slice simulation by GPGPU, *Ultramicroscopy*, 2015, **158**, 56–64.

22 E. Epifanovsky, A. T. B. Gilbert, X. Feng, J. Lee, Y. Mao, N. Mardirossian, P. Pokhilko, A. F. White, M. P. Coons, A. L. Dempwolff, Z. Gan, D. Hait, P. R. Horn, L. D. Jacobson, I. Kaliman, J. Kussmann, A. W. Lange, K. U. Lao, D. S. Levine, J. Liu, S. C. McKenzie, A. F. Morrison, K. D. Nanda, F. Plasser, D. R. Rehn, M. L. Vidal, Z.-Q. You, Y. Zhu, B. Alam, B. J. Albrecht, A. Aldossary, E. Alguire, J. H. Andersen, V. Athavale, D. Barton, K. Begam, A. Behn, N. Bellonzi, Y. A. Bernard, E. J. Berquist, H. G. A. Burton, A. Carreras, K. Carter-Fenk, R. Chakraborty, A. D. Chien, K. D. Closser, V. Cofer-Shabica, S. Dasgupta, M. de Wergifosse, J. Deng, M. Diedenhofen, H. Do, S. Ehlert, P.-T. Fang, S. Fatehi, Q. Feng, T. Friedhoff, J. Gayvert, Q. Ge, G. Gidofalvi, M. Goldey, J. Gomes, C. E. González-Espinoza, S. Gulania, A. O. Gunina, M. W. D. Hanson-Heine, P. H. P. Harbach, A. Hauser, M. F. Herbst, M. H. Vera, M. Hodecker, Z. C. Holden, S. Houck, X. Huang, K. Hui, B. C. Huynh, M. Ivanov, Á. Jász, H. Ji, H. Jiang, B. Kaduk, S. Kähler, K. Khistyaev, J. Kim, G. Kis, P. Klunzinger, Z. Koczor-Benda, J. H. Koh, D. Kosenkov, L. Koulias, T. Kowalczyk, C. M. Krauter, K. Kue, A. Kunitsa, T. Kus, I. Ladjánszki, A. Landau, K. V. Lawler, D. Lefrancois, S. Lehtola, R. R. Li, Y.-P. Li, J. Liang, M. Liebenthal, H.-H. Lin, Y.-S. Lin, F. Liu, K.-Y. Liu, M. Loipersberger, A. Luenser, A. Manjanath, P. Manohar, E. Mansoor, S. F. Manzer, S.-P. Mao, A. V. Marenich, T. Markovich, S. Mason, S. A. Maurer, P. F. McLaughlin, M. F. S. J. Menger, J.-M. Mewes, S. A. Mewes, P. Morgante, J. W. Mullinax, K. J. Oosterbaan, G. Paran, A. C. Paul, S. K. Paul, F. Pavošević, Z. Pei, S. Prager, E. I. Proynov, Á. Rák, E. Ramos-Cordoba, B. Rana, A. E. Rask, A. Rettig, R. M. Richard, F. Rob, E. Rossomme, T. Scheele, M. Scheurer, M. Schneider, N. Sergueev, S. M. Sharada, W. Skomorowski, D. W. Small, C. J. Stein, Y.-C. Su, E. J. Sundstrom, Z. Tao, J. Thirman, G. J. Tornai, T. Tsuchimochi, N. M. Tubman, S. P. Veccham, O. Vydrov, J. Wenzel, J. Witte, A. Yamada, K. Yao, S. Yeganeh, S. R. Yost, A. Zech, I. Y. Zhang, X. Zhang, Y. Zhang, D. Zuev, A. Aspuru-Guzik, A. T. Bell, N. A. Besley, K. B. Bravaya, B. R. Brooks, D. Casanova, J.-D. Chai, S. Coriani, C. J. Cramer, G. Cserey, A. E. DePrince, R. A. DiStasio, A. Dreuw, B. D. Dunietz, T. R. Furlani, W. A. Goddard, S. Hammes-Schiffer, T. Head-Gordon, W. J. Hehre, C.-P. Hsu, T.-C. Jagau, Y. Jung, A. Klamt, J. Kong, D. S. Lambrecht, W. Liang, N. J. Mayhall, C. W. McCurdy, J. B. Neaton, C. Ochsenfeld, J. A. Parkhill, R. Peverati, V. A. Rassolov, Y. Shao, L. V. Slipchenko, T. Stauch, R. P. Steele, J. E. Subotnik, A. J. W. Thom, A. Tkatchenko, D. G. Truhlar, T. V. Voorhis, T. A. Wesolowski, K. B. Whaley, H. L. Woodcock, P. M. Zimmerman, S. Faraji, P. M. W. Gill, M. Head-Gordon, J. M. Herbert and A. I. Krylov, Software for the frontiers of quantum chemistry: an overview of developments in the Q-Chem 5 package, *J. Chem. Phys.*, 2021, **155**, 084801.

23 Y. Shao, Z. Gan, E. Epifanovsky, A. T. B. Gilbert, M. Wormit, J. Kussmann, A. W. Lange, A. Behn, J. Deng, X. Feng, D. Ghosh, M. Goldey, P. R. Horn, L. D. Jacobson, I. Kaliman, R. Z. Khaliullin, T. Kuś, A. Landau, J. Liu, E. I. Proynov, Y. M. Rhee, R. M. Richard, M. A. Rohrdanz, R. P. Steele, E. J. Sundstrom, H. L. Woodcock, P. M. Zimmerman, D. Zuev, B. Albrecht, E. Alguire, B. Austin, G. J. O. Beran, Y. A. Bernard, E. Berquist, K. Brandhorst, K. B. Bravaya, S. T. Brown, D. Casanova, C.-M. Chang, Y. Chen, S. H. Chien, K. D. Closser, D. L. Crittenden, M. Diedenhofen, R. A. DiStasio, H. Do, A. D. Dutoi, R. G. Edgar, S. Fatehi, L. Fusti-Molnar, A. Ghysels, A. Golubeva-Zadorozhnaya, J. Gomes, M. W. D. Hanson-Heine, P. H. P. Harbach, A. W. Hauser, E. G. Hohenstein, Z. C. Holden, T.-C. Jagau, H. Ji, B. Kaduk, K. Khistyaev, J. Kim, J. Kim, R. A. King, P. Klunzinger, D. Kosenkov, T. Kowalczyk, C. M. Krauter, K. U. Lao, A. D. Laurent, K. V. Lawler, S. V. Levchenko, C. Y. Lin, F. Liu, E. Livshits, R. C. Lochan, A. Luenser, P. Manohar, S. F. Manzer, S.-P. Mao, N. Mardirossian, A. V. Marenich, S. A. Maurer, N. J. Mayhall, E. Neuscamman, C. M. Oana, R. Olivares-Amaya, D. P. O'Neill, J. A. Parkhill, T. M. Perrine, R. Peverati, A. Prociuk, D. R. Rehn, E. Rosta, N. J. Russ, S. M. Sharada, S. Sharma, D. W. Small, A. Sodt, T. Stein, D. Stück, Y.-C. Su, A. J. W. Thom, T. Tsuchimochi, V. Vanovschi, L. Vogt, O. Vydrov, T. Wang, M. A. Watson, J. Wenzel, A. White, C. F. Williams, J. Yang, S. Yeganeh, S. R. Yost, Z.-Q. You, I. Y. Zhang, X. Zhang, Y. Zhao, B. R. Brooks, G. K. L. Chan, D. M. Chipman, C. J. Cramer, W. A. Goddard, M. S. Gordon, W. J. Hehre, A. Klamt, H. F. Schaefer, M. W. Schmidt, C. D. Sherrill, D. G. Truhlar, A. Warshel, X. Xu, A. Aspuru-Guzik, R. Baer, A. T. Bell, N. A. Besley, J.-D. Chai, A. Dreuw, B. D. Dunietz, T. R. Furlani, S. R. Gwaltney, C.-P. Hsu, Y. Jung, J. Kong, D. S. Lambrecht, W. Liang, C. Ochsenfeld, V. A. Rassolov, L. V. Slipchenko, J. E. Subotnik, T. V. Voorhis, J. M. Herbert, A. I. Krylov, P. M. W. Gill and M. Head-Gordon, Advances in molecular quantum chemistry contained in the Q-Chem 4 program package, *Mol. Phys.*, 2015, **113**, 184–215.

24 Y. Shao, L. F. Molnar, Y. Jung, J. Kussmann, C. Ochsenfeld, S. T. Brown, A. T. B. Gilbert, L. V. Slipchenko, S. V. Levchenko,

D. P. O'Neill, R. A. D. Jr, R. C. Lochan, T. Wang, G. J. O. Beran, N. A. Besley, J. M. Herbert, C. Y. Lin, T. V. Voorhis, S. H. Chien, A. Sodt, R. P. Steele, V. A. Rassolov, P. E. Maslen, P. P. Korambath, R. D. Adamson, B. Austin, J. Baker, E. F. C. Byrd, H. Dachsel, R. J. Doerksen, A. Dreuw, B. D. Dunietz, A. D. Dutoi, T. R. Furlani, S. R. Gwaltney, A. Heyden, S. Hirata, C.-P. Hsu, G. Kedziora, R. Z. Khalliulin, P. Klunzinger, A. M. Lee, M. S. Lee, W. Liang, I. Lotan, N. Nair, B. Peters, E. I. Proynov, P. A. Pieniazek, Y. M. Rhee, J. Ritchie, E. Rosta, C. D. Sherrill, A. C. Simmonett, J. E. Subotnik, H. L. W. III, W. Zhang, A. T. Bell, A. K. Chakraborty, D. M. Chipman, F. J. Keil, A. Warshel, W. J. Hehre, H. F. S. III, J. Kong, A. I. Krylov, P. M. W. Gill and M. Head-Gordon, Advances in methods and algorithms in a modern quantum chemistry program package, *Phys. Chem. Chem. Phys.*, 2006, **8**, 3172–3191.

25 J. J. P. Stewart, Optimization of parameters for semiempirical methods V: modification of NDDO approximations and application to 70 elements, *J. Mol. Model.*, 2007, **13**, 1173–1213.

26 J.-D. Chai and M. Head-Gordon, Long-range corrected hybrid density functionals with damped atom–atom dispersion corrections, *Phys. Chem. Chem. Phys.*, 2008, **10**, 6615–6620.

27 Y. Minenkov, Å. Singstad, G. Occhipinti and V. R. Jensen, The accuracy of DFT-optimized geometries of functional transition metal compounds: a validation study of catalysts for olefin metathesis and other reactions in the homogeneous phase, *Dalton Trans.*, 2012, **41**, 5526–5541.

28 V. A. Rassolov, M. A. Ratner, J. A. Pople, P. C. Redfern and L. A. Curtiss, 6-31G* basis set for third-row atoms, *J. Comput. Chem.*, 2001, **22**, 976–984.

29 S. G. Wang and W. H. E. Schwarz, Density functional study of first row transition metal dihalides, *J. Chem. Phys.*, 1998, **109**, 7252–7262.

30 R. Ditchfield, W. J. Hehre and J. A. Pople, Self-Consistent Molecular-Orbital Methods. IX. An Extended Gaussian-Type Basis for Molecular-Orbital Studies of Organic Molecules, *J. Chem. Phys.*, 1971, **54**, 724–728.

31 T. Clark, J. Chandrasekhar, G. W. Spitznagel and P. V. R. Schleyer, Efficient diffuse function-augmented basis sets for anion calculations. III. The 3-21+G basis set for first-row elements, Li–F, *J. Comput. Chem.*, 1983, **4**, 294–301.

32 R. Krishnan, J. S. Binkley, R. Seeger and J. A. Pople, Self-consistent molecular orbital methods. XX. A basis set for correlated wave functions, *J. Chem. Phys.*, 1980, **72**, 650–654.

33 A. Liu, H. Zhu, T. Zou, Y. Reo, G.-S. Ryu and Y.-Y. Noh, Evaporated nanometer chalcogenide films for scalable high-performance complementary electronics, *Nat. Commun.*, 2022, **13**, 6372.

34 X. Wang, Y. Hu, S. Y. Kim, R. Addou, K. Cho and R. M. Wallace, Origins of Fermi Level Pinning for Ni and Ag Metal Contacts on Tungsten Dichalcogenides, *ACS Nano*, 2023, **17**, 20353–20365.

35 R. K. Biroju, P. Harrison, W. Theis, N. V. Rees, R. Sharma, T. N. Narayanan and M. G. Hahm, Pt147 Nanoclusters Soft-Landed on WS2 Nanosheets for Catalysis and Energy Harvesting, *ACS Appl. Nano Mater.*, 2021, **4**, 13140–13148.

36 M. Kim, S. Nabeya, S.-M. Han, M.-S. Kim, S. Lee, H.-M. Kim, S.-Y. Cho, D.-J. Lee, S.-H. Kim and K.-B. Kim, Selective Atomic Layer Deposition of Metals on Graphene for Transparent Conducting Electrode Application, *ACS Appl. Mater. Interfaces*, 2020, **12**, 14331–14340.

37 J. Feng, X. Gong, X. Lou and R. G. Gordon, Direct-Liquid-Evaporation Chemical Vapor Deposition of Nanocrystalline Cobalt Metal for Nanoscale Copper Interconnect Encapsulation, *ACS Appl. Mater. Interfaces*, 2017, **9**, 10914–10920.

38 S. Lee, W. Lee, H.-T. Jung and C. A. Ross, Selective Deposition of Copper on Self-Assembled Block Copolymer Surfaces *via* Physical Vapor Deposition, *ACS Appl. Mater. Interfaces*, 2021, **13**, 52931–52937.

39 T. Shimizu, D. Lungerich, J. Stuckner, M. Murayama, K. Harano and E. Nakamura, Real-Time Video Imaging of Mechanical Motions of a Single Molecular Shuttle with Sub-Millisecond Sub-Angstrom Precision, *Bull. Chem. Soc. Jpn.*, 2020, **93**, 1079–1085.

40 J. Biskupek, S. T. Skowron, C. T. Stoppiello, G. A. Rance, S. Alom, K. L. Y. Fung, R. J. Whitby, M. H. Levitt, Q. M. Ramasse, U. Kaiser, E. Besley and A. N. Khlobystov, Bond Dissociation and Reactivity of HF and H2O in a Nano Test Tube, *ACS Nano*, 2020, **14**, 11178–11189.

41 S. Okada, S. Kowashi, L. Schweighauser, K. Yamanouchi, K. Harano and E. Nakamura, Direct Microscopic Analysis of Individual C60 Dimerization Events: Kinetics and Mechanisms, *J. Am. Chem. Soc.*, 2017, **139**, 18281–18287.

42 T. Nakamuro, K. Kamei, K. Sun, J. W. Bode, K. Harano and E. Nakamura, Time-Resolved Atomistic Imaging and Statistical Analysis of Daptomycin Oligomers with and without Calcium Ions, *J. Am. Chem. Soc.*, 2022, **144**, 13612–13622.

43 H. Hanayama, J. Yamada, K. Harano and E. Nakamura, Cyclodextrins as Surfactants for Solubilization and Purification of Carbon Nanohorn Aggregates, *Chem. – Asian J.*, 2020, **15**, 1549–1552.

44 T. Nakamuro, M. Sakakibara, H. Nada, K. Harano and E. Nakamura, Capturing the Moment of Emergence of Crystal Nucleus from Disorder, *J. Am. Chem. Soc.*, 2021, **143**, 1763–1767.

45 K. Jia, J. Zhang, L. Lin, Z. Li, J. Gao, L. Sun, R. Xue, J. Li, N. Kang, Z. Luo, M. H. Rummeli, H. Peng and Z. Liu, Copper-Containing Carbon Feedstock for Growing Superclean Graphene, *J. Am. Chem. Soc.*, 2019, **141**, 7670–7674.

46 X. Li, W. Cai, L. Colombo and R. S. Ruoff, Evolution of Graphene Growth on Ni and Cu by Carbon Isotope Labeling, *Nano Lett.*, 2009, **9**, 4268–4272.

47 J. Robertson, Amorphous carbon, *Adv. Phys.*, 1986, **35**, 317–374.

48 J. Zhao, Q. Deng, S. M. Avdoshenko, L. Fu, J. Eckert and M. H. Rümmeli, Direct in situ observations of single Fe atom catalytic processes and anomalous diffusion at graphene edges, *Proc. Natl. Acad. Sci. U. S. A.*, 2014, **111**, 15641–15646.

49 T. Furnival, R. K. Leary, E. C. Tyo, S. Vajda, Q. M. Ramasse, J. M. Thomas, P. D. Bristowe and P. A. Midgley, Anomalous

diffusion of single metal atoms on a graphene oxide support, *Chem. Phys. Lett.*, 2017, **683**, 370–374.
50 C. Gong, A. W. Robertson, K. He, C. Ford, A. A. R. Watt and J. H. Warner, Interactions of Pb and Te atoms with graphene, *Dalton Trans.*, 2014, **43**, 7442–7448.
51 K. Murakami, Y. Yamamoto, H. Yorimitsu and A. Osuka, Demetalation of Metal Porphyrins *via* Magnesium Porphyrins by Reaction with Grignard Reagents, *Chem. – Eur. J.*, 2013, **19**, 9123–9126.
52 J. A. Cowan and J. K. M. Sanders, Reductive demetallation of porphyrins: evidence for peripheral and axial modes of reduction, *Tetrahedron Lett.*, 1986, **27**, 1201–1204.
53 M. Kumar, P. Neta, T. P. G. Sutter and P. Hambright, One-electron reduction and demetallation of copper porphyrins, *J. Phys. Chem.*, 1992, **96**, 9571–9575.
54 T. Susi, J. C. Meyer and J. Kotakoski, Quantifying transmission electron microscopy irradiation effects using two-dimensional materials, *Nat. Rev. Phys.*, 2019, **1**, 397–405.
55 S. T. Skowron, T. W. Chamberlain, J. Biskupek, U. Kaiser, E. Besley and A. N. Khlobystov, Chemical Reactions of Molecules Promoted and Simultaneously Imaged by the Electron Beam in Transmission Electron Microscopy, *Acc. Chem. Res.*, 2017, **50**, 1797–1807.
56 R. F. Egerton, P. Li and M. Malac, Radiation damage in the TEM and SEM, *Micron*, 2004, **35**, 399–409.
57 A. Jablonski, F. Salvat, C. J. Powell and A. Y. Lee, *NIST Electron Elastic-Scattering Cross-Section Database Version 4.0*, NIST Standard Reference Database Number 64, National Institute of Standards and Technology, 2016.
58 R. F. Egerton, Mechanisms of radiation damage in beam-sensitive specimens, for TEM accelerating voltages between 10 and 300 kV, *Microsc. Res. Tech.*, 2012, **75**, 1550–1556.
59 D. Liu, S. Kowashi, T. Nakamuro, D. Lungerich, K. Yamanouchi, K. Harano and E. Nakamura, Ionization and electron excitation of C60 in a carbon nanotube: a variable temperature/voltage transmission electron microscopic study, *Proc. Natl. Acad. Sci. U. S. A.*, 2022, **119**, e2200290119.
60 D. Liu, D. Lungerich, T. Nakamuro, K. Harano and E. Nakamura, Excited state modulation of C70 dimerization in a carbon nanotube under a variable electron acceleration voltage, *Micron*, 2022, **160**, 103316.
61 A. S. Sinitsa, T. W. Chamberlain, T. Zoberbier, I. V. Lebedeva, A. M. Popov, A. A. Knizhnik, R. L. McSweeney, J. Biskupek, U. Kaiser and A. N. Khlobystov, Formation of Nickel Clusters Wrapped in Carbon Cages: Toward New Endohedral Metallofullerene Synthesis, *Nano Lett.*, 2017, **17**, 1082–1089.
62 I. V. Lebedeva, T. W. Chamberlain, A. M. Popov, A. A. Knizhnik, T. Zoberbier, J. Biskupek, U. Kaiser and A. N. Khlobystov, The atomistic mechanism of carbon nanotube cutting catalyzed by nickel under an electron beam, *Nanoscale*, 2014, **6**, 14877–14890.
63 C. S. Tian, D. Qian, D. Wu, R. H. He, Y. Z. Wu, W. X. Tang, L. F. Yin, Y. S. Shi, G. S. Dong, X. F. Jin, X. M. Jiang, F. Q. Liu, H. J. Qian, K. Sun, L. M. Wang, G. Rossi, Z. Q. Qiu and J. Shi, Body-Centered-Cubic Ni and Its Magnetic Properties, *Phys. Rev. Lett.*, 2005, **94**, 137210.
64 C. Han, S. Yang, K. G. Chang, P. P. Wang, R. Murakami and X. P. Song, Structure transition and magnetism of bcc-Ni nanowires, *J. Mater. Chem. C*, 2014, **3**, 1004–1010.
65 T. Shimizu, D. Lungerich, K. Harano and E. Nakamura, Time-Resolved Imaging of Stochastic Cascade Reactions over a Submillisecond to Second Time Range at the Angstrom Level, *J. Am. Chem. Soc.*, 2022, **144**, 9797–9805.
66 H. Hölzel, M. Muth, D. Lungerich and N. Jux, Addressing Environmental Challenges of Porphyrin Mixtures Obtained from Statistical Syntheses, *Chem. Methods*, 2021, **1**, 142–147.
67 M. Lepper, J. Köbl, L. Zhang, M. Meusel, H. Hölzel, D. Lungerich, N. Jux, A. de Siervo, B. Meyer, H. Steinrück and H. Marbach, Controlling the Self-Metalation Rate of Tetraphenylporphyrins on Cu(111) *via* Cyano Functionalization, *Angew. Chem., Int. Ed.*, 2018, **57**, 10074–10079.
68 D. Lungerich, J. F. Hitzenberger, W. Donaubauer, T. Drewello and N. Jux, Three Short Stories about Hexaarylbenzene–Porphyrin Scaffolds, *Chem. – Eur. J.*, 2016, **22**, 16755–16759.
69 M. Ruppel, D. Lungerich, S. Sturm, R. Lippert, F. Hampel and N. Jux, A Comprehensive Study on Tetraaryltetrabenzoporphyrins, *Chem. – Eur. J.*, 2020, **26**, 3287–3296.
70 M. Ruppel, L.-P. Gazetas, D. Lungerich, F. Hampel and N. Jux, Investigations of Low-Symmetrical Tetraaryltetrabenzoporphyrins Produced by Mixed Condensation Reactions, *J. Org. Chem.*, 2020, **85**, 7781–7792.